

POLARIMETRIC CALIBRATION OF PALSAR

PI 121

Hiroshi kimura

Dept. of Electrical and Electronic Eng., Gifu University

Abstract—For spaceborne polarimetric synthetic aperture radar (SAR), it is important to ensure the removal of both polarimetric system distortion and the effect of Faraday rotation. This paper proposes a new calibration method to derive the system distortion using polarization orientation (PO) induced in built-up areas and applies to Phased-Array-Type L-Band SAR (PALSAR) calibration. Faraday rotation is corrected by the circularpolarization-based method from the distortion matrix (DM)-calibrated data. The derived DMs do not coincide with those by the Japan Aerospace Exploration Agency (JAXA), but our calibration results compare well to JAXA's results in PO angles and calibrator's responses. The two results satisfy polarimetric calibration requirements, and the cross-polarized isolation improves by more than 5 dB after Faraday rotation correction following DM calibration—even in the case of small Faraday rotation (-2° to -0.5°). The proposed method is robust to noise and is useful when using an area of mixed polarimetric response for calibration. This method is also applicable to a large crosstalk system and the case of large Faraday rotation.

Index Terms—Faraday rotation, Phased-Array-Type L-Band Synthetic Aperture Radar (PALSAR), polarimetric calibration, polarization orientation (PO), urban area.

1. INTRODUCTION

The Phased Array type L-band Synthetic Aperture Radar (PALSAR) onboard the Japanese Advanced Land Observation Satellite (ALOS) has been successfully in orbit since January 2006. PALSAR has a quad-polarization (fully polarimetric) operation mode and full scattering matrix scenes have been provided to the user community. To extract relevant information about a target, polarimetric calibration focusing on removal of the polarimetric system distortion is necessary. Extensive efforts have been devoted to this matter. Polarimetric calibration methods available in the literature can be categorized into three major groups: 1) methods based on point targets with known scattering matrices [1]-[3]; 2) methods based on distributed targets with known scattering characteristics [4], [5]; and 3) methods that use one or more trihedral corner reflectors and natural targets [6]-[8][9]. At present, van Zyl's [7] and Quegan's [9]

methods belonging to the third group are widely applied to polarimetric calibration of airborne SARs, such as AIRSAR [10], EMISAR [11], E-SAR [12] and Pi-SAR [13], [14]. On the other hand, recently several new methods based on polarimetric characteristics of targets have been proposed. For example, one method uses symmetric target tilt angles [15], another introduces a concept of orientation angle preserving [16] and this author proposed a method to use polarization orientation angles in built-up areas [17].

In addition, PALSAR has a problem of Faraday rotation relating to low frequency (L-band). It is suggested that a Faraday rotation of $30\pm 10^\circ$ provides a reasonable explanation of some anomalous scattering behavior observed by JERS-1 L-band SAR over the Amazon rainforest [18]. One-way Faraday rotations exceeding 5° are likely to significantly reduce the accuracy of geophysical parameter recovery, while at solar maximum, 75% of the orbit is affected by one-way Faraday rotation over 5° [19]. The maximum value for Faraday rotation angle is estimated to be 40° at L-band; the Faraday rotation may be a significant source of measurement error even if the system distortion is well-calibrated [20]. Therefore, polarimetric calibration of PALSAR is more critical than that of an airborne SAR. Recently methods to estimate and correct Faraday rotation were studied [21] and a robust method is shown in [22] and [23].

This author proposed a new approach using polarization orientation angles in built-up areas for polarimetric calibration including Faraday rotation correction [17] and [24]. In the following section, we apply this new approach to calibrate the polarimetric PALSAR system. A system distortion model including Faraday rotation is addressed in Section 2. The calibration approach using polarization orientation, calibration equations and separation of the system distortion matrices and Faraday rotation angles are described in Section 3. The PALSAR calibration result is presented in Section 4.

2. SYSTEM MODEL AFFECTED BY FARADAY ROTATION

The polarimetric PALSAR system affected by Faraday

rotation can be modeled as the following nonreciprocal distortion system:

$$\mathbf{O} = \mathbf{RFSFT} + \mathbf{N}$$

$$= \begin{bmatrix} r_{11} & r_{12} \\ r_{21} & r_{22} \end{bmatrix} \begin{bmatrix} \cos\Omega & \sin\Omega \\ -\sin\Omega & \cos\Omega \end{bmatrix} \begin{bmatrix} S_{hh} & S_{hv} \\ S_{vh} & S_{vv} \end{bmatrix} \begin{bmatrix} \cos\Omega & \sin\Omega \\ -\sin\Omega & \cos\Omega \end{bmatrix} \quad (1)$$

$$+ \begin{bmatrix} t_{11} & t_{12} \\ t_{21} & t_{22} \end{bmatrix} + \begin{bmatrix} n_{hh} & n_{hv} \\ n_{vh} & n_{vv} \end{bmatrix}$$

where \mathbf{O} is the observed scattering matrix, \mathbf{S} is the Scattering matrix, \mathbf{F} represents the one-way Faraday rotation matrix [19] and [21], \mathbf{R} and \mathbf{T} are the receive and transmit distortion matrices, respectively, and \mathbf{N} is the noise matrix. The matrices \mathbf{R} and \mathbf{T} include cross-talk (off-diagonal) terms r_{ij} and t_{ij} ($i \neq j$), which are usually expected to be small compared to the diagonal terms r_{ii} and t_{ii} , but are not neglected in this article. A Faraday rotation angle Ω in the matrix \mathbf{F} is approximated by [19]

$$\Omega = KN_f B \cos\psi \sec\theta_0 / f^2 \quad [\text{radians}] \quad (2)$$

Where K is constant of value 2.365×10^4 , N_f is the total electron content (TEC) in TEC units (TECU) of 10^{16} electrons per square meter, B is the magnetic flux density in Tesla, ψ and θ_0 are the angles the wave normal makes with the earth's magnetic field and the downward vertical respectively, and f is frequency in Hz. The magnetic field factor $B \cos\psi \sec\theta_0$ is calculated at a constant height of 400 km. In this article, we define the unit horizontal polarization vector h as $v \times k$ from the unit vertical polarization vector and the unit incident direction vector (see Fig. 1). The incidence plane is defined by the line of sight direction and by the z axis (i.e., the y - z plane in Fig. 1). In (1), the positive Faraday rotation is defined in a clockwise direction when looking toward the radar.

Equation (1) can be rewritten as

$$\mathbf{O} = \mathbf{R}_F \mathbf{S} \mathbf{T}_F + \mathbf{N}$$

$$= \begin{bmatrix} r_{F11} & r_{F12} \\ r_{F21} & r_{F22} \end{bmatrix} \begin{bmatrix} S_{hh} & S_{hv} \\ S_{vh} & S_{vv} \end{bmatrix} \begin{bmatrix} t_{F11} & t_{F12} \\ t_{F21} & t_{F22} \end{bmatrix} + \begin{bmatrix} n_{hh} & n_{hv} \\ n_{vh} & n_{vv} \end{bmatrix} \quad (3)$$

$$\mathbf{R}_F = \mathbf{R}\mathbf{F} = \begin{bmatrix} r_{F11} & r_{F12} \\ r_{F21} & r_{F22} \end{bmatrix}$$

$$= \begin{bmatrix} r_{11} \cos\Omega - r_{12} \sin\Omega & r_{11} \sin\Omega + r_{12} \cos\Omega \\ r_{21} \cos\Omega - r_{22} \sin\Omega & r_{21} \sin\Omega + r_{22} \cos\Omega \end{bmatrix} \quad (4)$$

$$\mathbf{T}_F = \mathbf{T}\mathbf{F} = \begin{bmatrix} t_{F11} & t_{F12} \\ t_{F21} & t_{F22} \end{bmatrix}$$

$$= \begin{bmatrix} t_{11} \cos\Omega + t_{21} \sin\Omega & t_{12} \cos\Omega + t_{22} \sin\Omega \\ t_{21} \cos\Omega - t_{11} \sin\Omega & t_{22} \cos\Omega - t_{12} \sin\Omega \end{bmatrix}$$

where \mathbf{R}_F and \mathbf{T}_F are combined matrices of Faraday rotation and the receive and transmit distortion, respectively (equivalent distortion matrices). This has the same form of (1) with no Faraday rotation, which is the case of an airborne SAR system. The diagonal terms of the matrices \mathbf{R} and \mathbf{T} are usually very large compared to the off-diagonal terms. However, the off-diagonal terms of the matrices \mathbf{R}_F and \mathbf{T}_F increases when the Faraday rotation angle increases. These terms have the same effect of the increase of cross-talk. If the additive noise is

negligible, calibration can be equivalently carried out using the following equation:

$$\mathbf{S}_c = \mathbf{R}_F^{-1} \mathbf{O} \mathbf{T}_F^{-1} \quad (5)$$

Given the matrices \mathbf{R}_F and \mathbf{T}_F and the Faraday rotation angle Ω , the matrices \mathbf{R} , \mathbf{T} and \mathbf{F} can be derived from the relation of (4), and then

$$\mathbf{S}_c = \mathbf{F}^{-1} \mathbf{R}^{-1} \mathbf{O} \mathbf{T}^{-1} \mathbf{F}^{-1} \quad (6)$$

3. POLARIMETRIC CALIBRATION USING POLARIZATION ORIENTATION

The methods in [6]–[9] classified into the third group in Section I are widely used for polarimetric calibration, but they employ several assumptions such as small system cross-talk, scattering reciprocity and complete uncorrelation between the co- and cross-polarized backscatter of azimuthal symmetric targets. In addition, Quegan's method expects areas used for calibration to have much larger co-polarized backscatter than the cross-polarized one. In reality, the careful selection of calibration areas is often required. When Faraday rotation increases, the equivalent system cross-talk increases. Even with a zero cross-talk system, the Faraday rotation angle of 5° induces an equivalent -15 dB cross-talk from (1). Therefore these methods must have problems under Faraday rotation due to deviation from the assumptions. In this section, we introduce a new method to calibrate polarimetric SAR using polarization orientation in built-up areas. The polarization orientation in built-up areas is briefly reviewed, followed by the derivation of equivalent distortion matrices, separation of Faraday rotation and calibration of general scenes.

A. Polarization Orientation in Built-up Areas

The polarization orientation angle is defined as the angle between the major axis of the polarization ellipse and the horizontal polarization axis. It is known that terrain slopes induce a polarization angle shift θ , which is the angle that rotates the incidence plane about the line-of-sight to the surface normal by the following equation [25]:

$$\tan\theta = \frac{\tan\omega}{-\tan\gamma \cos\phi + \sin\phi} \quad (7)$$

where $\tan\omega$ is the azimuth slope, $\tan\gamma$ is the slope in ground range direction, and ϕ is the radar incidence angle. The incident direction and the vertical polarization are in the incidence plane. Note that ω is positive when the azimuth slope lies in the first and third quadrants of the h - v plane and negative when it lies in the second and fourth quadrants.

For polarimetric data represented by scattering matrix

$$\mathbf{S} = \begin{bmatrix} S_{hh} & S_{hv} \\ S_{vh} & S_{vv} \end{bmatrix} \quad (8)$$

The measured scattering matrix after the rotation by θ is

$$\tilde{\mathbf{S}} = \begin{bmatrix} \cos \theta & -\sin \theta \\ \sin \theta & \cos \theta \end{bmatrix} \mathbf{S} \begin{bmatrix} \cos \theta & \sin \theta \\ -\sin \theta & \cos \theta \end{bmatrix}. \quad (9)$$

Note that in this article the direction of the rotation is opposite to [25] and [26].

Lee *et al.* compared three estimators of the polarization orientation angle and attributed the soundness of the circular polarization method [26]. It can be explained by the fact that this algorithm employs only an assumption of reflection symmetry. The covariance matrix gives the following relation:

$$\langle \tilde{S}_{rr} \tilde{S}_{ll}^* \rangle = \langle S_{rr} S_{ll}^* \rangle e^{j4\theta} \quad (10)$$

where $\langle \rangle$ indicates averaging. Note that the argument in (10) is opposite to that in [26] due to the definition of θ (9). For a reflection symmetrical medium, $\langle S_{rr} S_{ll}^* \rangle$ becomes real in value

$$\langle S_{rr} S_{ll}^* \rangle = \left(-\langle |S_{hh} - S_{vv}|^2 \rangle + 4\langle |S_{hv}|^2 \rangle \right) / 4. \quad (11)$$

For scattering from sloping natural terrain (11) is normally negative [26], therefore the estimate of orientation angle by the circular polarization method is

$$\theta = \text{Arg} \left(-\langle \tilde{S}_{rr} \tilde{S}_{ll}^* \rangle \right) / 4. \quad (12)$$

Polarization orientation angle shifts can be seen not only in rugged terrain but also urban areas. Those in built-up areas can be explained by double-bounce scattering ground-wall and wall-ground. From the scattering model of built-up areas, the polarization orientation angle shift in built-up areas is given as [27] and [28]

$$\tan \theta = \frac{-\tan \alpha}{\cos \phi} \quad (13)$$

where α is the wall or street orientation angle, and ϕ is the radar incidence angle (see Fig. 1). This relation suggests that urban scatterers are in reflection symmetry.

B. Derivation of the distortion matrices

The basis of our calibration method is very simple and is that two polarization orientation angles from the two combinations of polarizations (HH, VV and HV) and (HH, VV and VH) must be identical after calibration in built-up areas [17] and [24]. Here we need not know a value of the true polarization orientation angle. The two circular components are

$$\begin{aligned} \tilde{S}_{rr} &= (\tilde{S}_{hh} - \tilde{S}_{vv} + j2\tilde{S}_{xy}) / 2, \\ \tilde{S}_{ll} &= (\tilde{S}_{vv} - \tilde{S}_{hh} + j2\tilde{S}_{xy}) / 2 \end{aligned} \quad (14)$$

We have two possibilities for \tilde{S}_{xy} , that is \tilde{S}_{hv} and \tilde{S}_{vh} . Therefore, the following must be satisfied after calibration in built-up areas.

$$\text{Arg} \left(\langle \tilde{S}_{rr} \tilde{S}_{ll}^* \rangle_{hv} \right) = \text{Arg} \left(\langle \tilde{S}_{rr} \tilde{S}_{ll}^* \rangle_{vh} \right) \quad (15)$$

where the suffix xy of $\langle \rangle$ indicates that the xy component is used. This is similar to identical cross-polarized backscatter but not exactly, because the polarization orientation angle is a function of three linear polarizations.

The proposed method to derive distortion matrices has the following schemes. After calibration,

1. Two possible polarization orientation angles in built-up areas must be identical,
2. In built-up areas, reciprocity is satisfied and two sets of cross-polarized power are same under a high S/N state,
3. Correlation between the co- and cross-polarized backscatter for surface scattering targets not always becomes zero, but small,
4. For trihedral corner reflectors and/or other standard targets, co-polarized channels are balanced.

So far urban areas have not been considered as calibration targets, but the proposed method uses them positively. An advantage of this method is its robustness to noise. In contrast to other well-known methods [6]-[9], this method does not impose a complete uncorrelation between the co- and cross-polarized backscatter for surface scattering targets and a small system cross-talk. According to the above schemes, we introduce the following functions using the calibrated scattering matrix terms:

$$\begin{aligned} f_1 &= \sum_{BA} |\gamma(S_{crr}, S_{crl})_{hv} - \gamma(S_{crr}, S_{crl})_{vh}| \\ &\quad + |\text{sgn}(\theta)_{hv} - \text{sgn} \theta| + |\text{sgn}(\theta)_{vh} - \text{sgn} \theta| \\ f_2 &= \sum_{BA} \left| \langle S_{chv} / S_{cvh} \rangle - 1 \right|^2 \\ f_3 &= \sum_{SS} \left[|\gamma(S_{chh}, S_{chv})| + |\gamma(S_{cqv}, S_{chv})| + |\gamma(S_{chh}, S_{cvh})| + |\gamma(S_{cqv}, S_{cvh})| \right] \\ f_4 &= \sum_{SC} w \left[|S_{chh} / S_{cqv} - 1| + 1 / \log_{10} |S_{chh}| + 1 / \log_{10} |S_{cqv}| \right] / N_{SC} \\ f &= f_1 + f_2 + f_3 + f_4 \end{aligned} \quad (16)$$

where BA , SS and SC mean built-up areas, surface scattering areas and standard calibrators respectively, θ is the polarization orientation angle, sgn is a sign function, w in f_4 is a weighting parameter (10 in this study), N_{SC} is the number of used calibrators (1 in this study) and $\gamma(u, v)$ represents the correlation coefficient between u and v

$$\gamma(u, v) = \langle uv^* \rangle / \sqrt{\langle uu^* \rangle \langle vv^* \rangle}. \quad (17)$$

The suffix xy of $\gamma(u, v)$ and $\langle \theta \rangle$ in f_1 indicates that the xy component is used to calculate them. Functions f_1 to f_4 correspond to the above schemes 1 to 4. For f_1 (scheme 1), cross-correlation coefficients are used instead of polarization orientation angles so that a built-up area with higher coherency gets more weight. The sgn function in f_1 is introduced to prevent them from running into opposite signed numbers. Again note that we don't need the precise value of each polarization orientation angle. The derivation of distortion matrices can be expressed as a minimization problem of the summed function f . To solve this problem, we employ simulated annealing [29], which is an iterative stochastic relaxation technique for the global optimization. This method has been known to have a relatively low risk of running into a local *minima*

compared to other optimization algorithms, and has been applied to various fields such as restoration of polarimetric SAR images [30], unwrapping of SAR interferograms [31], and atmospheric correction of hyperspectral data [32], among others. After simulated annealing optimization, the equivalent distortion matrices including Faraday rotation effects \mathbf{T}_F and \mathbf{R}_F are derived.

C. Separation of Faraday rotation angles and distortion matrices

We assume stable system distortion with PALSAR and a variable Faraday rotation angle depending on observation time i . From (4), it seems that given more than two sets of independent measurement of the equivalent system distortion matrices $\mathbf{T}_F(i)$ and $\mathbf{R}_F(i)$ ($i \geq 2$), the system distortion matrices \mathbf{T} and \mathbf{R} and the Faraday rotation angle $\Omega(i)$ could be separated. However, it is not the case.

The Faraday rotation angle can be written as,

$$\Omega(i) = \Omega_0 + \Omega_1(i). \quad (18)$$

where Ω_0 is a biased term and $\Omega_1(i)$ is a variable term at observation time i . From this, the one-way Faraday rotation matrix can be rewritten as,

$$\begin{aligned} \mathbf{F}(\Omega(i)) &= \begin{bmatrix} \cos(\Omega_0 + \Omega_1(i)) & \sin(\Omega_0 + \Omega_1(i)) \\ -\sin(\Omega_0 + \Omega_1(i)) & \cos(\Omega_0 + \Omega_1(i)) \end{bmatrix} \\ &= \begin{bmatrix} \cos\Omega_0 & \sin\Omega_0 \\ -\sin\Omega_0 & \cos\Omega_0 \end{bmatrix} \begin{bmatrix} \cos\Omega_1(i) & \sin\Omega_1(i) \\ -\sin\Omega_1(i) & \cos\Omega_1(i) \end{bmatrix}. \quad (19) \\ &= \mathbf{F}(\Omega_0)\mathbf{F}(\Omega_1(i)) \\ &= \begin{bmatrix} \cos\Omega_1(i) & \sin\Omega_1(i) \\ -\sin\Omega_1(i) & \cos\Omega_1(i) \end{bmatrix} \begin{bmatrix} \cos\Omega_0 & \sin\Omega_0 \\ -\sin\Omega_0 & \cos\Omega_0 \end{bmatrix} \\ &= \mathbf{F}(\Omega_1(i))\mathbf{F}(\Omega_0) \end{aligned}$$

These equations mean that the one-way Faraday rotation matrix $\mathbf{F}(\Omega(i))$ can be the product of two matrices $\mathbf{F}(\Omega_0)\mathbf{F}(\Omega_1(i))$ or $\mathbf{F}(\Omega_1(i))\mathbf{F}(\Omega_0)$. From (4) and (19), we have

$$\mathbf{R}_F(i) = \mathbf{R}\mathbf{F}(\Omega(i)) = \mathbf{R}\mathbf{F}(\Omega_0)\mathbf{F}(\Omega_1(i)) = \mathbf{R}_{F0}\mathbf{F}(\Omega_1(i)) \quad (20)$$

$$\mathbf{T}_F(i) = \mathbf{T}\mathbf{F}(\Omega(i)) = \mathbf{F}(\Omega_1(i))\mathbf{F}(\Omega_0)\mathbf{T} = \mathbf{F}(\Omega_1(i))\mathbf{T}_{F0}$$

where $\mathbf{R}_{F0} = \mathbf{R}\mathbf{F}(\Omega_0)$ and $\mathbf{T}_{F0} = \mathbf{F}(\Omega_0)\mathbf{T}$ are distortion matrices involving the bias term of Faraday rotation. Hence, if N sets of $\mathbf{T}_F(i)$ and $\mathbf{R}_F(i)$ are given ($N \geq 2$), \mathbf{T}_{F0} , \mathbf{R}_{F0} and $\Omega_1(i)$ ($i=1, \dots, N$) can be analytically resolved by a method such as a least square method.

Only in the case of $\Omega_0=0$, exact Faraday rotation angles are resolved because of $\Omega(i)=\Omega_1(i)$. However, that is not guaranteed. The number of pairs of Ω_0 and $\Omega_1(i)$ satisfying (18) will be innumerable. Solutions of Ω_0 and $\Omega_1(i)$ by a least square method will be converged to arbitrary values minimizing the least square error by chance. If one or some datasets are altered to others, the solutions Ω_0 and $\Omega_1(i)$ corresponding to remaining datasets may change. Therefore (20) means that unique separation of the Faraday rotation and the system distortion matrices is impossible in the presence of both

Faraday and system cross-talk effects. In this study, Ω_0 is differently estimated as shown in IV. When the bias term Ω_0 is determined, the system distortion matrices are

$$\begin{aligned} \mathbf{R} &= \mathbf{R}_{F0}\mathbf{F}^{-1}(\Omega_0), \\ \mathbf{T} &= \mathbf{F}^{-1}(\Omega_0)\mathbf{T}_{F0} \end{aligned} \quad (21)$$

D. Calibration of general scenes

Once the distortion matrices are determined, the calibration of general scenes can be performed in a straightforward way. System distortion is first removed from the observed data.

$$\mathbf{Z} = \mathbf{R}^{-1}\mathbf{O}\mathbf{T}^{-1} \quad (22)$$

Next, the Faraday rotation angle is estimated by the method based on the correlation of circular cross-polarizations [33], known as a robust method [22] and [23].

$$\begin{bmatrix} Z_{rr} & Z_{rl} \\ Z_{lr} & Z_{ll} \end{bmatrix} = \frac{1}{2} \begin{bmatrix} 1 & j \\ j & 1 \end{bmatrix} \begin{bmatrix} Z_{hh} & Z_{hv} \\ Z_{vh} & Z_{vv} \end{bmatrix} \begin{bmatrix} 1 & j \\ j & 1 \end{bmatrix} \quad (23)$$

$$\Omega = -\frac{1}{4} \arg(Z_{rl}Z_{lr}^*) \quad (24)$$

Finally, polarimetrically calibrated data removing the Faraday rotation is obtained.

$$\mathbf{S}_c = \mathbf{F}^{-1}(\Omega)\mathbf{Z}\mathbf{F}^{-1}(\Omega). \quad (25)$$

4. PALSAR CALIBRATION

The method described in III is applied to PALSAR scenes of JAXA's level 1.1 products calibrated by JAXA. Parameters of distortion matrices used for JAXA's calibration are stored in the leader file. Before applying our calibration method, JAXA's calibration was removed and uncalibrated scenes were recovered.

A. The system distortion

To derive sets of \mathbf{T}_F and \mathbf{R}_F , four calibration site scenes in Japan were used. One Tomakomai scene from a descending orbit contains a JAXA's 3 meter trihedral corner reflector as a calibrator. Three Gifu scenes from ascending orbits contain a 2 m trihedral corner reflector and a 1.0 m \times 3.6 m flat plate as calibrators. While the maximum RCS of a 2 m trihedral corner reflector is 30.6 dBm² for PALSAR (23.5 cm wavelength), that of a 1.0 m \times 3.6 m flat plate increases to 34.7 dBm². Taking into account that an azimuth of SAR illumination is much more stable than its elevation, the 1.0 m side was aligned with the range direction during deployment. The approximate half-power beam width is 1.9° in azimuth and 6.7° in range. Owing to a careful orienting the flat panel to the PALSAR's illumination direction, it was imaged more brightly than the trihedral corner reflector in all three Gifu scenes. The flat panel was therefore used as a calibrator for the Gifu scene.

The PALSAR scenes are displayed in Fig. 2. In the Gifu and Tomakomai scenes, ten 9×45 pixel and six 16×80 pixel areas are respectively selected in both built-up and low co- and cross-polarized correlation areas. Their locations are shown in Fig. 2. Built-up areas are selected so that the number of areas with positive and negative street orientation angles becomes the same, with their angles as far away from zero as possible. It is easy to discriminate positive and negative street orientations from street patterns in the PALSAR amplitude images. Furthermore, referring street maps will make certain it. Figs. 3(a) and 3(b) show two polarization orientation angles from an uncalibrated scene of Gifu and Tomakomai respectively, in which the difference of the two angles is obvious. To improve a throughput of the simulated annealing optimization, the following constraint is introduced expecting the small Faraday rotation and small cross-talk:

$$0.5 < |R_{F_{ii}}| < 1.5, |R_{F_{ij}}| < 0.2 (i \neq j), 0.5 < |T_{F_{ii}}| < 1.5 \text{ AND} \\ |T_{F_{ij}}| < 0.2 (i \neq j)$$

This must be changed in case of large Faraday rotation and/or large cross-talk. Four sets of distortion matrices, \mathbf{T}_F and \mathbf{R}_F , affected by the Faraday rotation obtained by each optimization differ from each other because of varied Faraday rotation effects.

Next, a least square method is applied to separate \mathbf{T}_{F0} , \mathbf{R}_{F0} and $\Omega_1(i)$ from four sets of \mathbf{T}_F and \mathbf{R}_F .

$$\mathbf{T}_{F0} = \begin{bmatrix} 1.0000 & 0.0241 + j0.0262 \\ -0.0305 + j0.0052 & 0.8982 + j0.4196 \end{bmatrix} \quad (26)$$

$$\mathbf{R}_{F0} = \begin{bmatrix} 1.0000 & -0.0509 + j0.0141 \\ 0.0285 + j0.0077 & 0.7237 + j0.0277 \end{bmatrix}$$

The four Faraday rotation angles Ω_1 are given in the third column of Table I. If estimates are good, these separated Faraday rotation angles should be equal to those found by the circular-polarization-based method ((23) and (24)) \mathbf{T}_{F0} and \mathbf{R}_{F0} calibrated scenes, shown in the fourth column of Table I. The maximum difference is 0.65° in the Tomakomai case.

As described in III-C, the bias term of the Faraday rotation angle Ω_0 may be nonzero. To estimate Ω_0 , we compare the Faraday rotation angle from (2) and the scene-dependent term Ω_1 . This calculation is performed not only for the four calibration scenes in Japan (in the Northern Hemisphere), but also the four Amazonian scenes (near the Equator) and four Australian scenes (in the Southern Hemisphere) obtained between May 2006 and October 2007. Among the 12 scenes, one Tomakomai and two Amazonian scenes are from descending orbits, and the rest are from ascending orbits. Using (2), the TEC value and the geomagnetic field were derived from the International Reference Ionosphere (IRI-2001) and the International Geomagnetic Reference Field (IGRF),

respectively. Fig. 4 shows a good linear relationship between Ω and Ω_1 , expressed by

$$\Omega = 1.050\Omega_1 - 0.713 \text{ (degrees)} \quad (27)$$

with $R^2 = 0.787$ and an almost 1.0 slope. This equation supports validity of the relationship (18) and yields the estimate $\Omega_0 = -0.713$ degrees. Hence, the final solutions of the PALSAR system distortion matrices by the proposed method are

$$\mathbf{T} = \mathbf{F}^{-1}(\Omega_0)\mathbf{F}(\Omega_0)\mathbf{T} \\ = \begin{bmatrix} 1.0000 & 0.0353 + j0.0314 \\ -0.0429 + j0.0052 & 0.8983 + j0.4194 \end{bmatrix} \quad (28)$$

$$\mathbf{R} = \mathbf{R}\mathbf{F}(\Omega_0)\mathbf{F}^{-1}(\Omega_0) \\ = \begin{bmatrix} 1.0000 & -0.0384 + j0.0141 \\ 0.0195 + j0.0074 & 0.7235 + j0.0279 \end{bmatrix}$$

For reference, JAXA's distortion matrices are

$$\mathbf{T}_{(JAXA)} = \begin{bmatrix} 1.0000 & 0.0024 + j0.0129 \\ -0.0115 - j0.0062 & 0.9572 + j0.3830 \end{bmatrix} \quad (29)$$

$$\mathbf{R}_{(JAXA)} = \begin{bmatrix} 1.0000 & -0.0063 + j0.0071 \\ -0.0063 + j0.0080 & 0.7217 - j0.0237 \end{bmatrix}$$

B. Calibration results

The derived PALSAR system distortion matrices by the proposed method differ from those by JAXA. In this section, 12 scenes are calibrated and the results are compared for the following cases:

- 1) uncalibration (UN),
- 2) distortion matrix (DM) calibration, applying (22) and (28) or JAXA L1.1, and
- 3) distortion matrix and Faraday rotation calibration (DMF), applying (23)-(25) to the DM case, viz., (22)-(25) and (28).

Faraday rotation angles are estimated in the DMF case from (23) and (24). Fig. 5 shows a comparison of the derived Faraday rotation angles from JAXA L1.1 products and those from DM-calibrated scenes using our method. Note that the angles by our method coincide with those by JAXA within a difference of -0.03° to -0.04° .

Figs. 3(c) and 3(d) show the two orientation angles of Gifu and Tomakomai scenes for the DM case using our method. Compared with the angles from the uncalibrated scenes (Figs. 3(a) and 3(b)), the consistency of the two angles dramatically improves after calibration. Fig. 6 shows the average difference of two polarization orientation angles of 12 scenes for three cases. Figs. 6(a) and 6(b) show the mean and standard deviation, respectively, and indicate a significant decrease in the difference between the two angles and its deviation after calibration and a slight difference between our method and JAXA. The improvement in the DMF case over the DM case is not recognizable. Thus the two polarization orientation angles of the DMF case by our method and

those of the DM and DMF cases by JAXA are not depicted here.

Another good index of calibration quality is a calibrator's response. The average of the four calibration site scenes was examined. The average co-polarized amplitude balance shown in Fig. 7(a) is -0.08 dB for our calibration and 0.23 dB for JAXA calibration for both the DM and DMF cases. The average co-polarized phase balance shown in Fig. 7(b) is 0.2° for our calibration and -6.3° for JAXA calibration for both the DM and DMF cases. Remarkable improvement after calibration is obvious in both our method and JAXA's as shown in Fig. 7(a) and Fig. 7(b). The difference between the DM and DMF cases appears in the cross-polarized isolation of the calibrator as shown in Fig. 7(c). The Faraday rotation calibration following DM calibration improves by more than 5 dB in average in the cross-polarized isolation compared to DM calibration only. The Faraday rotation angles range -2° to -0.5° as shown in Fig. 5. This suggests the advantage of Faraday rotation calibration even if the angle is as small as a few degrees. The values from the calibrator's response satisfy or almost satisfy the CEOS CAL/VAL Working group polarimetric calibration requirements as shown in Table II [34]. Conclusive differences between the obtained results and JAXA's were not found for the calibrator's responses as well as the derived Faraday rotation angles and the two polarization orientation angles.

5. CONCLUSION

A new calibration method using polarization orientation induced in built-up areas is proposed and applied to PALSAR polarimetric calibration. Its fundamental concept is simple: two polarization orientation angles from two polarization combinations should be identical after calibration. Distributed targets and a standard calibrator response are also used in the calibration process as well as other typical calibration methods. The proposed method avoids an assumption of a small cross-talk system, and employs additional assumptions of only backscattering reciprocity of built-up areas and low (nonzero) correlation between the co- and cross-polarized backscatter from surface scattering areas. With the help of built-up areas (which have high SNR), this method is robust to noise. In this article, we apply a simulated annealing optimization and there are still more options to resolve calibration parameters. The derived system distortion matrices do not coincide with those by JAXA, but a comparison of calibration results shows good similarity with respect to polarization orientation angles and calibrator's responses. A possible reason for this is that the cross-talk terms of PALSAR are inherently very small. It was also shown that both results satisfy the polarimetric calibration requirements by the CEOS CAL/VAL Working group. In addition, Faraday rotation

angles can be derived by the circular-polarization-based method from the DM-calibrated data and its correction improves cross-polarized isolation by more than 5 dB even in case of small Faraday rotation (-2° to -0.5°). The proposed method is robust to noise and useful when using an area of mixed polarimetric response for calibration. Furthermore, this method could be applicable to a large cross-talk system and the case of large Faraday rotation.

6. ACKNOWLEDGMENT

The author would like to thank the Japan Aerospace Exploration Agency for the acquisition and provision of the PALSAR data. The used TEC values and geomagnetic fields were obtained from <http://ccmc.gsfc.nasa.gov/modelweb/models/iri.html> and <http://swdcwww.kugi.kyoto-u.ac.jp/igrf/point/index-j.html>, respectively.

7. REFERENCES

- [1] A. Freeman, Y. Shen, and C. L. Werner, "Polarimetric SAR calibration experiment using active radar calibrators," *IEEE Trans. Geosci. Remote Sens.*, vol. 28, no. 2, pp. 224–240, Mar. 1990.
- [2] K. Sarabandi, L. E. Pierce, and F. T. Ulaby, "Calibration of a polarimetric imaging SAR," *IEEE Trans. Geosci. Remote Sens.*, vol. 30, no. 3, pp. 540–549, May 1992.
- [3] M. Fujita, T. Masuda, Y. Fujino, and M. Satake, "Polarimetric calibration of the SIR-C C-band channel using active radar calibrators and polarization selective dihedrals," *IEEE Trans. Geosci. Remote Sens.*, vol. 36, no. 6, pp. 1872–1878, Nov. 1998.
- [4] K. Sarabandi, "Calibration of a polarimetric synthetic aperture radar using a known distributed target," *IEEE Trans. Geosci. Remote Sens.*, vol. 32, no. 3, pp. 575–582, May 1994.
- [5] K. Sarabandi, L. E. Pierce, Y. Oh, M. C. Dobson, F. T. Ulaby, A. Freeman, and P. Dubois, "Cross-calibration experiment of JPL AIRSAR and truckmounted polarimetric scatterometer," *IEEE Trans. Geosci. Remote Sens.*, vol. 32, no. 5, pp. 975–985, Sep. 1994.
- [6] J. D. Klein, "Calibration of complex polarimetric SAR imagery using backscatter correlations," *IEEE Trans. Aerosp. Electron. Syst.*, vol. 28, no. 1, pp. 183–194, Jan. 1992.
- [7] J. J. van Zyl, "Calibration of polarimetric radar images using only image parameters and trihedral corner reflector responses," *IEEE Trans. Geosci. Remote Sens.*, vol. 28, no. 3, pp. 337–348, May 1990.
- [8] A. Freeman, J. J. van Zyl, J. D. Klein, H. A. Zebker, and Y. Shen, "Calibration of Stokes and scattering matrix format polarimetric SAR data," *IEEE Trans. Geosci. Remote Sens.*, vol. 30, no. 3, pp. 531–539, May 1992.
- [9] S. Quegan, "A unified algorithm for phase and cross-

- talk calibration of polarimetric data—Theory and observations,” *IEEE Trans. Geosci. Remote Sens.*, vol. 32, no. 1, pp. 89–99, Jan. 1994.
- [10] J. J. van Zyl, C. F. Bumette, H. A. Zebker, A. Freeman, and J. Holt, *POLCAL User’s Manual*. Pasadena, CA: JPL, Aug. 1990.
- [11] E. L. Christensen, N. Skou, J. Dall, K. W. Woelders, J. H. Jørgensen, J. Granholm, and S. N. Madsen, “EMISAR: An absolutely calibrated polarimetric L- and C-band SAR,” *IEEE Trans. Geosci. Remote Sens.*, vol. 36, no. 6, pp. 1852–1865, Nov. 1998.
- [12] R. Horn, R. Scheiber, S. Buckreuss, M. Zink, A. Moreira, E. Sansosti, and R. Lanari, “E-SAR generates level-3 SAR products for ProSmart,” in *Proc. IGARSS*, Hamburg, Germany, Jul. 1999, pp. 1195–1199.
- [13] National Institute of Information and Communication Technology, *Calibration of X-band*. (in Japanese). [Online]. Available: <http://www2.nict.go.jp/y/y221/pdf/kousei.pdf>
- [14] Japan Aerospace Exploration Agency, *Calibration*. (in Japanese). [Online]. Available: http://www.eorc.jaxa.jp/ALOS/Pi-SAR/ForPI/cal_val.html
- [15] R. Touzi and M. Shimada, “Polarimetric PALSAR calibration,” *IEEE Trans. Geosci. Remote Sens.*, vol. 47, no. 12, pp. 3951–3959, Dec. 2009.
- [16] T. L. Ainsworth, L. Ferro-Famil, and J.-S. Lee, “Orientation angle preserving a posteriori polarimetric SAR calibration,” *IEEE Trans. Geosci. Remote Sens.*, vol. 44, no. 4, pp. 994–1003, Apr. 2006.
- [17] H. Kimura, “Calibration of ALOS/PALSAR polarimetric data affected by Faraday rotation,” in *Proc. IGARSS*, Seoul, Korea, Jul. 2005, pp. 3369–3372.
- [18] E. Rignot, “Effect of Faraday rotation on L-band interferometric and polarimetric synthetic-aperture radar data,” *IEEE Trans. Geosci. Remote Sens.*, vol. 38, no. 1, pp. 383–390, Jan. 2000.
- [19] P. A. Wright, S. Quegan, N. S. Wheadon, and C. D. Hall, “Faraday rotation effects on L-band spaceborne SAR data,” *IEEE Trans. Geosci. Remote Sens.*, vol. 41, no. 12, pp. 2735–2744, Dec. 2003.
- [20] A. Freeman and S. S. Saatchi, “On the detection of Faraday rotation in linearly polarized L-band SAR backscatter signatures,” *IEEE Trans. Geosci. Remote Sens.*, vol. 42, no. 8, pp. 1607–1616, Aug. 2004.
- [21] A. Freeman, “Calibration of linearly polarized polarimetric SAR data subject to Faraday rotation,” *IEEE Trans. Geosci. Remote Sens.*, vol. 42, no. 8, pp. 1617–1624, Aug. 2004.
- [22] F. J. Meyer and J. B. Nicoll, “Prediction, detection, and correction of Faraday rotation in full-polarimetric L-band SAR data,” *IEEE Trans. Geosci. Remote Sens.*, vol. 46, no. 10, pp. 3076–3086, Oct. 2008.
- [23] J. S. Lee, K. S. Chen, T. L. Ainsworth, P. Bernhardt, M. Yamamoto, M. Ishii, Y. Otsuka, and L. C. Tsai, “Ionospheric structure imaging with ALOS PALSAR,” in *Proc. 1st Joint PI Symp. ALOS Data Nodes ALOS Sci. Program*, Kyoto, Japan, Nov. 2007.
- [24] H. Kimura, “Calibration of spaceborne polarimetric SAR data using polarization orientation,” in *Proc. IGARSS*, Denver, CO, Jul. 2006, pp. 344–347.
- [25] J. S. Lee, D. L. Schuler, and T. L. Ainsworth, “Polarimetric SAR data compensation for terrain azimuth slope variation,” *IEEE Trans. Geosci. Remote Sens.*, vol. 38, no. 5, pp. 2153–2163, Sep. 2000.
- [26] J. S. Lee, D. L. Schuler, T. L. Ainsworth, E. Krogager, D. Kasilingam, and W.-M. Boerner, “On the estimation of radar polarization orientation shifts induced by terrain slopes,” *IEEE Trans. Geosci. Remote Sens.*, vol. 40, no. 1, pp. 30–41, Jan. 2002.
- [27] H. Kimura, K. P. Papathanassiou, and I. Hajnsek, “Polarization orientation effects in urban areas on SAR data,” in *Proc. IGARSS*, Seoul, Korea, Jul. 2005, pp. 4863–4867.
- [28] H. Kimura, “Radar polarization orientation shifts in built-up areas,” *IEEE Geosci. Remote Sens. Lett.*, vol. 5, no. 2, pp. 217–221, Apr. 2008.
- [29] S. Kirkpatrick, C. D. Gelatt, Jr., and M. P. Vecchi, “Optimization by simulated annealing,” *Science*, vol. 220, no. 4598, pp. 671–680, May 1983.
- [30] J. Schou and H. Skriver, “Restoration of polarimetric SAR images using simulated annealing,” *IEEE Trans. Geosci. Remote Sens.*, vol. 39, no. 9, pp. 2005–2016, Sep. 2001.
- [31] S. Gudmundsson, J. M. Carstensen, and F. Sigmundsson, “Unwrapping ground displacement signals in satellite radar interferograms with aid of GPS data and MRF regularization,” *IEEE Trans. Geosci. Remote Sens.*, vol. 40, no. 8, pp. 1743–1754, Aug. 2002.
- [32] R. Marion, R. Michel, and C. Faye, “Atmospheric correction of hyperspectral data over dark surfaces via simulated annealing,” *IEEE Trans. Geosci. Remote Sens.*, vol. 44, no. 6, pp. 1566–1574, Jun. 2006.
- [33] S. H. Bickel and R. H. T. Bates, “Effects of magneto-ionic propagation on the polarization scattering matrix,” *Proc. IRE*, vol. 53, no. 8, pp. 1089–1091, Aug. 1965.
- [34] *Recommendations from CEOS CAL/VAL*. (2004). [Online]: Available: http://earth.esa.int/workshops/ceos_sar_2004/recommendation_at_ceos_cal.htm

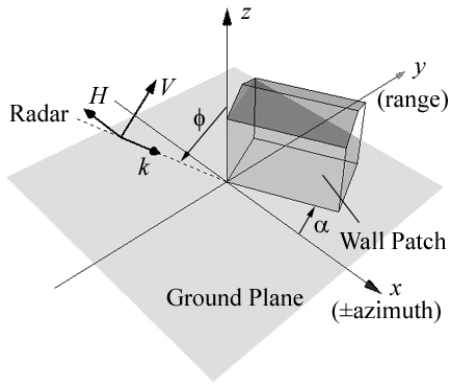


Fig. 1 Schematic diagram of the radar imaging geometry showing the orientation angle of house/building wall.



(a) (b)

Fig. 2 PALSAR scenes displayed with Pauli matrix components: $|HH-VV|$, $|HV|$, and $|HH + VV|$, for red, green, and blue, respectively. In both, the range is from right to left, and the azimuth is from top to bottom. Yellow and red boxes represent locations of samples for low co- and cross-polarized correlation and built-up areas, respectively. (a) Gifu and (b) Tomakomai. Spacing in the azimuth is scaled to 1/5 in (a) and 1/6 in (b) from JAXA L1.1 products to retain natural look.

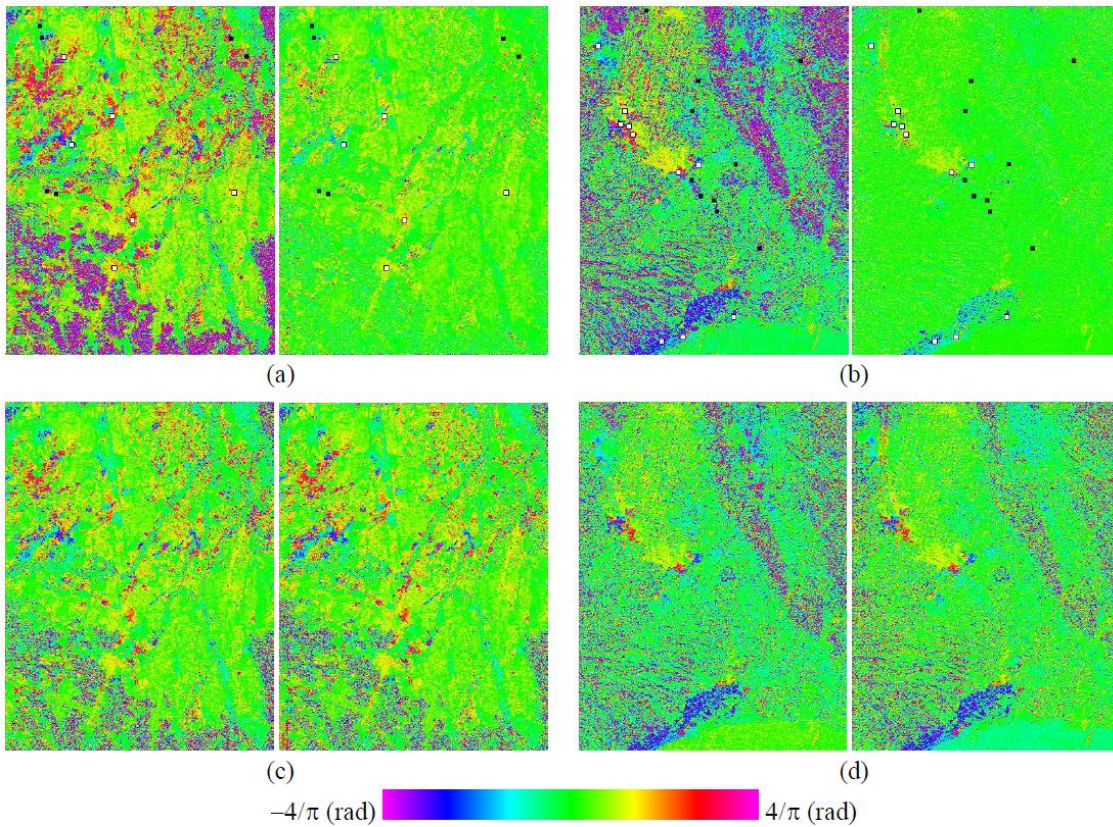


Fig. 3 Comparison of two polarization orientation angles. (a) Gifu uncalibrated scene. (b) Tomakomai uncalibrated scene. (c) Gifu T_F and R_F calibrated scene. (d) Tomakomai T_F and R_F calibrated scene. Left: angles from the combination of HH, VV and HV. Right: angles from the combination of HH, VV and VH. Black and white boxes in (a) and (b) correspond to yellow and red boxes in Fig. 2(a) and 2(b).

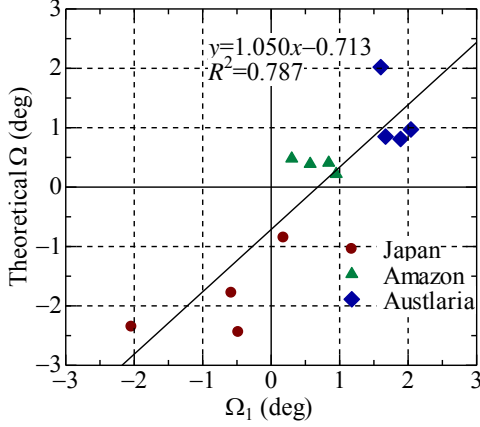


Fig. 4 Relationship between Ω computed from (2) and Ω_1 derived from \mathbf{T}_{F0} and \mathbf{R}_{F0} calibrated scenes.

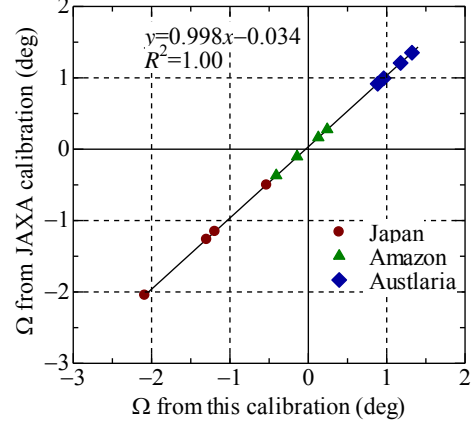


Fig. 5 Comparison of Faraday rotation angles derived from JAXA L1.1 products and those from distortion matrix (DM)-calibrated scenes by our method.

TABLE I: Comparison of separated Faraday rotation angles and estimated ones after \mathbf{T}_{F0} and \mathbf{R}_{F0} calibration

Scene	Date	Ω_1 Separated [degree]	Ω_1 Estimated after \mathbf{T}_{F0} and \mathbf{R}_{F0} Calibration [degree]
Gifu	2006/6/11	-0.47	-0.48
Gifu	2007/3/14	-0.16	0.18
Gifu	2007/4/29	-0.69	-0.58
Tomakomai	2006/5/19	-1.39	-2.04

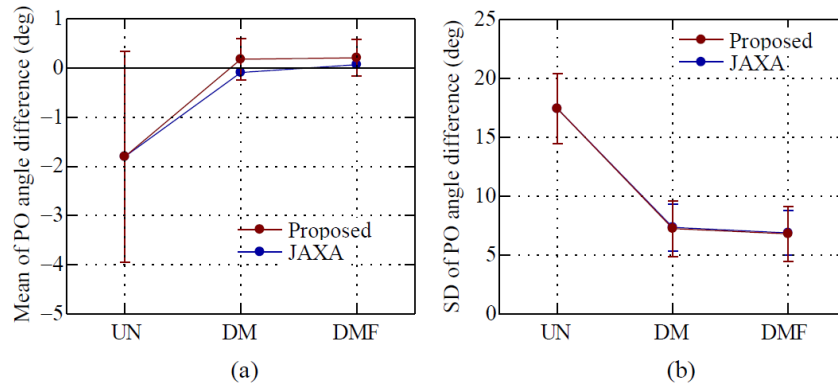


Fig. 6 Average difference of two polarization orientation (PO) angles of 12 scenes from uncalibrated scenes (UN), distortion matrix calibrated scenes (DM), and distortion matrix plus Faraday rotation calibrated scenes (DMF). (a) mean. (b) standard deviation.

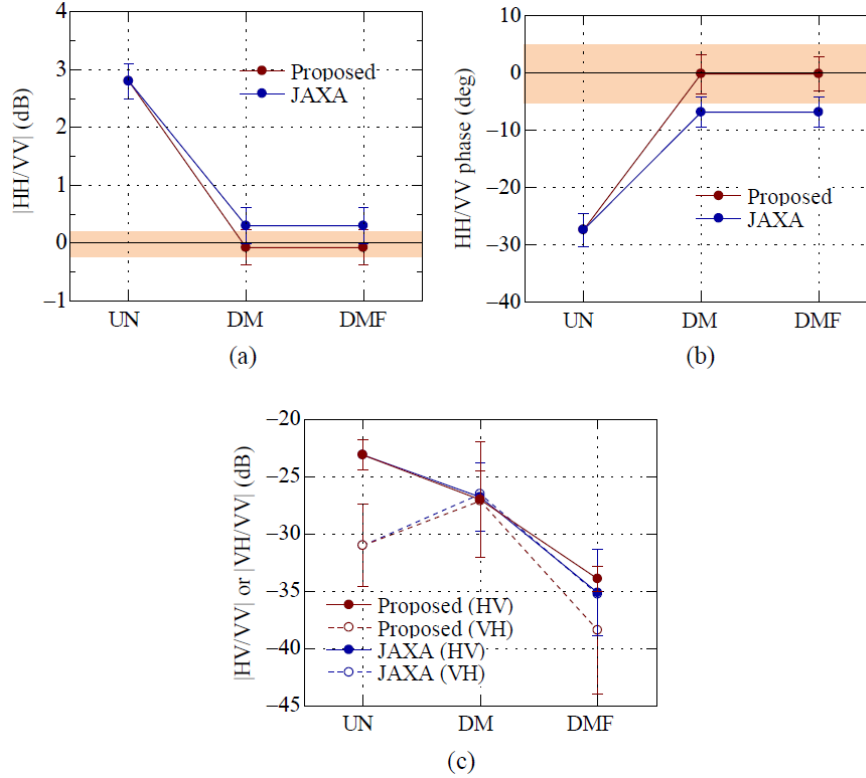


Fig. 7. Average of calibrator's responses of four calibration sites from uncalibrated scenes (UN), DM-calibrated scenes (DM), and DMplus Faraday rotation calibrated scenes (DMF). (a) Mean copolarized amplitude balance. (b) Mean copolarized phase balance. (c) Mean cross-polarized isolation.

TABLE II: Calibration requirements for polarimetry and interferometry [34]

ITEM	VALUE
CROSS-TALK	< -35 DB
CHANNEL AMPLITUDE IMBALANCE	0.2 DB (SOIL MOISTURE)
CHANNEL-PHASE	2° - 5°
FARADAY ROTATION CORRECTION	2.5° (L-BAND)